

Hybrid PIC-Fluid Simulation of a Waveguide ECR Magnetic Nozzle Plasma Thruster

M. R. Inchingolo¹, M. Merino¹ and J. Navarro¹

¹Equipo de Propulsión Espacial y Plasmas, Universidad Carlos III de Madrid, Leganés, Spain, minching@pa.uc3m.es

KEYWORDS: ECR thruster, Magnetic Nozzle, particle-in-cell plasma simulations.

ABSTRACT:

A circular waveguide electron-cyclotron resonance plasma thruster (ECRT) is simulated using a quasi-neutral 2D axisymmetric hybrid PIC-fluid code. The ECR region is modeled as an heating term in the energy equation for the electron fluid using two different power absorption maps. The main trends in the plasma discharge are evaluated, pointing out the importance of the electron temperature distribution in the plasma transport and the pressure gradient in determining the magnetic force. A parametric study on the propellant mass flow rate and deposited power is performed for one of the two power absorption maps, showing that the transport physics is mainly affected by the deposited energy per particle. A first estimate of the performance metrics is presented showing quantities in agreement with currently available experimental data for other ECRTs.

1 INTRODUCTION

Having been the most successful electric propulsion technology for half a century, Hall effect and Ion thruster are still the predominant technology[1]. The limited lifetime of hollow cathodes and grids is the primary concern for these type of thrusters[2], thus recently the interest in electrodeless plasma thruster has been constantly growing.

The electron cyclotron resonance thruster (ECRT) is an electrode-less plasma thruster that exploits the ECR resonance to efficiently couple electromagnetic power to the electrons of a plasma immersed in a magnetic field[3, 4]. This phenomenon is localized where the magnetic field is such that the electron cyclotron frequency coincides with the frequency of the applied electromagnetic wave. In order to create thrust, the ions are then accelerated by a magnetic nozzle as the electrons expansion creates an ambipolar field. In this process, a quasi-neutral plume is generated without the need of an external neutralizer.

Studies with waveguide coupled ECRT concepts started in the 1960's[5–7], with thrusters in the kW power range and microwave frequency of 8.35GHz. Different geometries and propellants such as mercury, were tested, never reaching thruster efficiencies greater than 6%, and experiencing many technolog-

ical challenges [7]. Similar results were obtained in more recent studies (1990's)[8–10] where an efficiency of 2% was estimated for a 500W class thruster working at 2.1GHz. In this case the low efficiency was attributed to unknown losses and imprecise microwave coupling measurements. Recently, within the European MINOTOR project [11–13] a novel coaxial ECRT thruster geometry was developed at ONERA and reached efficiencies above 16%(2.45GHz, 30W and 1sscm of Xenon) [13], thus further pushing the interest in the ECRT concept. However, the coaxial thruster suffers the erosion of the central conductor reducing again, the lifetime.

In 2019, the PROMETEO project has been instituted to exploit synergically the accumulated knowledge of the nuclear fusion and electric propulsion communities, involving the CIEMAT National Fusion Laboratory (LNF) and the Electric Space Propulsion research group (EP2-UC3M). In the frame of this project, EP2 is developing a new waveguide ECRT experiment, as a means to unravel the physics of electrodeless thrusters. An ECRT offers, in fact, the opportunity to achieve a better understanding on many plasma phenomena under study in both communities, namely, plasma transport, turbulence and wave-plasma interaction. The new ECRT here presented, has been designed with the objective of understanding with the current technological level and models, why limitations were experienced in the past with the waveguide ECRT and how they can be overcome.

As a fundamental step in the design process, it is necessary to model and simulate the plasma discharge. Different quasi-1D models were proposed in the past [10, 14, 15] obtaining in some cases good estimations of the thruster performance [15]. Recently, an axisymmetric full-wave 2D code (HYPHEN-ECRT/SURFET)[16, 17] has been used at EP2, in the frame of the mentioned MINOTOR project[18], to support the design of the ECRT developed at ONERA and improve its current physical understanding.

No effort instead has, to date, been made to simulate with a 2D model the circular waveguide ECRT concept. This paper, aims to address this aspect by simulating the EP2 ECRT prototype using the HYPHEN simulation platform. The lack of implementation of the $m = \pm 1$ wave propagation mode in a circular waveguide, for the current HYPHEN version, has been mitigated by prescribing the power deposition profile near the ECR region. This ap-

proach, while not self-consistent, provides a preliminary understanding of the discharge physics of the new ECRT. In particular, this paper tries to assess at what extent the power deposition profile, the ECR region position, and the operating point affect the thrust and plasma transport variables in the magnetic nozzle and what are the thruster performances to be expected in the upcoming experiments.

This paper is organized as follows. The physical design of the waveguide ECRT is treated in section 2. In section 3 the numerical model is described as well as the power absorption profile used for the simulations. In section 4 the results of this study are presented, and finally in section 5 the conclusions and some final considerations are discussed.

2 THRUSTER DESIGN

The waveguide ECRT described next is being developed within the EP2 group at UC3M in the framework of the PROMETEO project.

It is a fully electrode-less circular waveguide thruster. A cross-section of the thruster is represented in fig. 1. The plasma source region, where the injected gas is ionized, consists of a semi-opened metallic tube covered with a Boron-Nitride sleeve, with one end closed by a quartz backplate. The plasma source has an internal diameter 36 mm and length 20 mm and it is immersed in a static simply diverging magnetic field produced by a permanent magnet and can be tuned using a coil positioned around the plasma chamber. The permanent magnet is composed by twelve Sm2Co17 YXG-32 magnets assembled together to obtain a radially magnetized ring magnet with dimensions of 52 mm inner diameter, 140 mm outer diameter and 44 mm of width. In fig. 2a the magnetic field produced by this magnet can be visualized.

The propellant (initially Xenon, although other gases will be investigated) is injected radially from holes on the lateral walls positioned at $z = 2$ mm (being $z = 0$ at the front side of the quartz plate, and positive z pointing downstream to the external region). Microwave power at $f_{MW} = 5.8\text{GHz}$ enters the waveguide from the backplate side. At the position where the magnetic field strength reaches $B_{res} = 0.2\text{T}$ the resonance phenomenon takes place, this happens approximately at $z_{res} = 12\text{mm}$.

The thruster is designed to work in the range of microwave power $P_a = 100 - 300\text{W}$ with a mass flow rate range of $\dot{m}_p = 1 - 3\text{mg/s}$. These ranges will be the ones used for the simulations performed in this study.

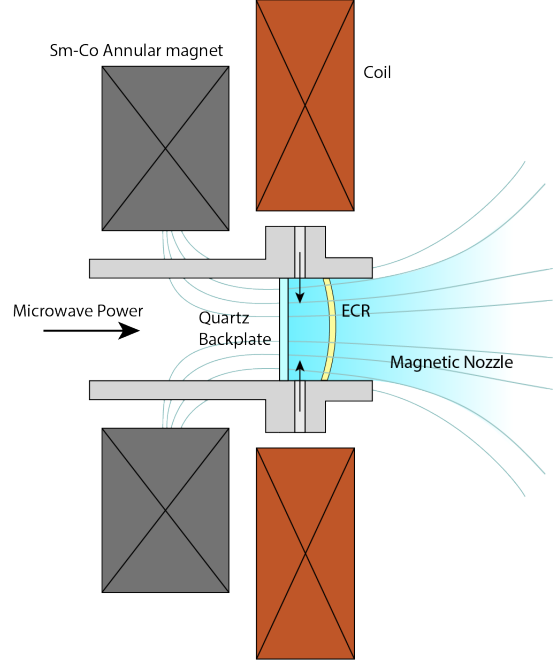


Figure 1: Simplified sketch of the ECR thruster being developed at UC3M (Drawing not in scale).

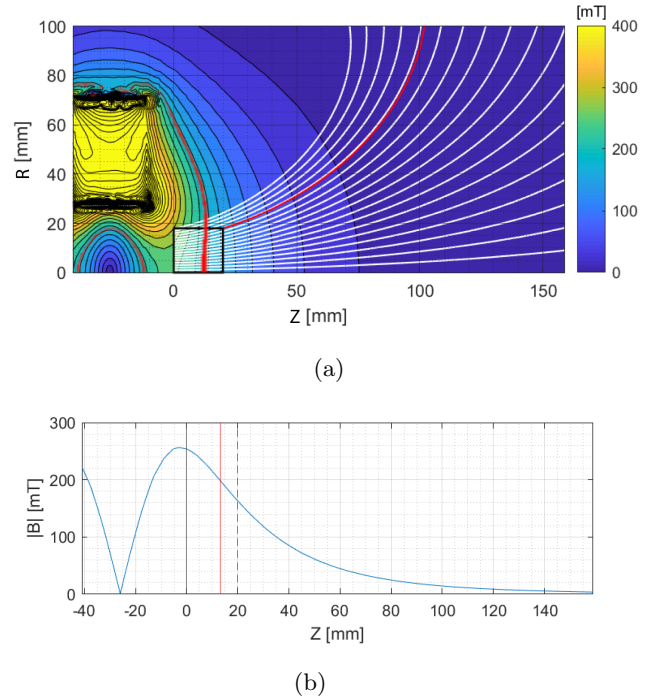


Figure 2: (a) 2D map of the magnetic field produced by the ring magnet assembly. The curves in red represent the magnetic field lines starting from the exit plane of the plasma source and the position of the resonance. (b) Magnetic field magnitude along the thruster axis. The thruster backplate is visible as a black solid line, the thruster exit plane as a dashed line and resonance mean position as a red line.

3 ECRT MODEL AND SIMULATION SETUP

The model used to assess the expected key aspects of the plasma transport as well as the propulsive performances of this ECRT prototype, is a two dimensional axisymmetric hybrid PIC-fluid code [19–21] created on the basis of previous plasma simulating platforms being developed within the EP2 team [22, 23]. In this code heavy particles (neutrals and ions) are modeled with a particle-in-cell kinetic model, whereas the electrons are treated as an anisotropic fluid. Because of the different models used for the two species, it is numerically convenient to operate on different types of spatial meshes [20, 24] and interpolate between them when required. A structured mesh is used for heavy species (PIC-mesh) and a non-structured magnetic field aligned mesh for the electrons (MFAM-mesh). Further details can be found in [19, 20, 25].

The basic simulation loop proceeds as follows. The PIC module takes as inputs the electric potential ϕ , the electron temperature T_e , and the electron current density \mathbf{j}_e , following a PIC scheme, these are used to propagate in time the trajectory of the heavy species and obtain the particle densities and fluxes, which in turn are the input for the electron fluid module. Here, imposing plasma quasi-neutrality, the continuity, momentum and energy equations are solved for the electron-fluid, obtaining \mathbf{j}_e , ϕ and T_e for the new time-step, thus closing the loop. Furthermore, in the electron-fluid loop the conditions at the plasma sheath (boundaries of the quasi-neutral domain) are calculated with a dedicated sheath submodule [20, 26]. The sheath module includes a specific set of modeling parameters for SEE and electron fluxes, in this work those of BN will be used. Further information about the sheath module and how SEE are modeled can be found in reference [20, 26]. Anomalous cross-field turbulent transport is instead modeled as a set of three empirical parameter in the momentum α_{tm} , energy α_{te} and heat flux α_{tq} equations of the fluid model. The settings here used consider all the three parameters as equal to $\alpha_{tm} = \alpha_{te} = \alpha_{tq} = 0.02$. More information on this empirical model can be found in [19, 27].

The code allows the selection of boundary conditions, domain geometries, collision types (excitation, primary and secondary ionisation, recombination, etc.), material surfaces and injection characteristics. The flexibility of this code makes it possible to simulate a number of different thrusters, such as Hall Effect Thrusters (HET) [19], Helicon Plasma thrusters (HPT) [28], coaxial ECRT thruster [17] or the waveguide ECRT object of this paper.

The working principle of an ECRT is based on the efficient microwave power absorption at the electron cyclotron resonance location. In this context, power absorption is modeled in the HYPHEN elec-

tron fluid module as an additional term Q_a in the electron internal energy equation (eq. 1).

$$\frac{\partial}{\partial t} \left(\frac{3}{2} n_e T_e \right) + \nabla \cdot \left(\frac{5}{2} n_e T_e \mathbf{u}_e + \mathbf{q}_e \right) = \mathbf{u}_e \cdot \nabla p_e + \sigma_e^{-1} \mathbf{j}_e \cdot (\mathbf{j}_e + \mathbf{j}_c) + Q_e + Q_a \quad (1)$$

Where n_e , T_e , \mathbf{u}_e , p_e , \mathbf{j}_e are respectively the electron density, the isotropic electron temperature, the electron fluid velocity, the electron pressure and the electron current density, while \mathbf{q}_e is the electron heat flux [19]. The electron parallel conductivity is defined as $\sigma_e = n_e e^2 / (m_e \nu_e)$ with m_e and ν_e the electron mass and electron collision frequency respectively, \mathbf{j}_c is a source term computed in the PIC module that takes into account the effect of electron collisions with the heavy species [19]. Concerning the terms Q_e and Q_a , the first represents the energy sink due to the ionization and excitation collisions, the latter, as mentioned, models the plasma-microwave absorption.

In order to determine the Q_a profile a wave module should be used, which would model the microwave propagation into the plasma by solving the Maxwell equations. This capability for a mode different than TEM ($m = 0$) [16, 17], such as the one propagating in a circular waveguide ($m = \pm 1$), is not yet implemented in this code and will be subject of future work. For this reason the Q_a spatial profile will be here assumed as described in section 3.1.

Fig. 3a describes the axisymmetric plasma domain used for all the simulations analyzed in this paper. The domain is divided into two regions, the plasma source and the plasma plume region. The plasma source region has dimensions of $R_T = 18\text{mm}$ and $L_T = 20\text{mm}$, whereas the plasma plume domain extends from $z = L_T$ to $z = L_D = 108\text{mm}$ and has an outer radius of $R_D = 54\text{mm}$. The injection is represented by a ring of injection surfaces positioned at $r = 18\text{mm}$, $z = 2\text{mm}$, with 2mm width, and the reference for the potential ϕ is positioned in a region with low numerical noise inside the plasma source.

The boundary surfaces of the simulations shown here, are of three types: Axisymmetric (B1), Dielectric (B2), Free Loss (B3). The B1 boundary consists of axisymmetric boundary conditions. B2 corresponds to the local zero-current condition $\mathbf{j}_e \cdot \mathbf{1}_n = -\mathbf{j}_i \cdot \mathbf{1}_n$, ion recombination, neutrals diffused reflection and $\mathbf{q}_e \cdot \mathbf{1}_n$ provided by the sheath module. On the free loss (B3) surfaces $\mathbf{j}_e \cdot \mathbf{1}_n = -\mathbf{j}_i \cdot \mathbf{1}_n$ and $\mathbf{q}_e \cdot \mathbf{1}_n = 2T_e n_e \mathbf{u}_e \cdot \mathbf{1}_n$, furthermore, the PIC macroparticles are removed from the simulation. These boundary conditions, make the external boundary locally current-free.

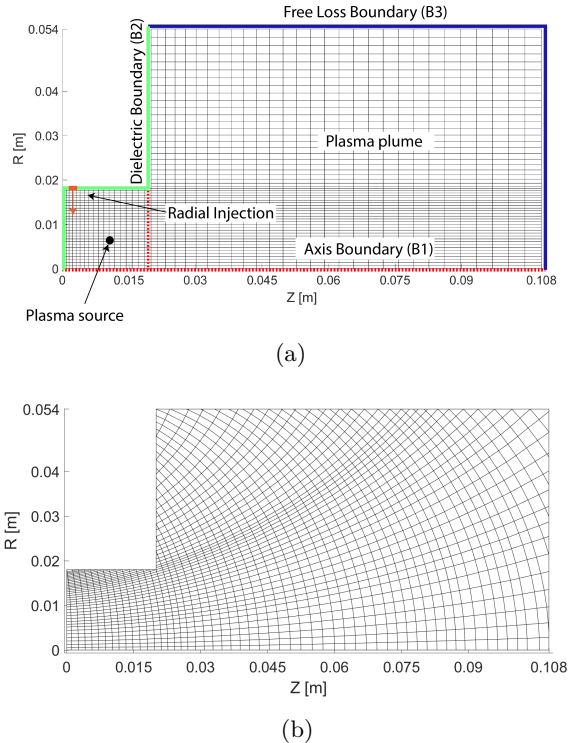


Figure 3: (a) PIC mesh and domain boundaries representation, (b) Magnetic field aligned mesh (MFAM).

The results shown here are obtained simulating neutral xenon atoms, singly- and doubly-ionized ions, thus they also include the effect of inelastic collisions such as single ionization, double ionization and excitation [19].

Fig. 3 shows the MFAM and PIC meshes used in the following sections. The MFAM mesh has been constructed with the iso-potential and stream lines of the magnetic field shown in fig. 2a and counts of about 1900 cells compared to the 2300 of the structured PIC-mesh. The typical cell size for both meshes is between 0.3mm^2 and 10mm^2 . A simulation of $t_{sim} = 5 \cdot 10^{-4}\text{s}$ of an ECR thruster with the above described settings, using a simulation time-step $dt = 2 \cdot 10^{-8}\text{s}$, takes about 9 hours to run on a workstation with ten cores of an Intel Xeon 6230 processor.

3.1 Power absorption profiles

Figures 4a and 4b show the two power deposition profiles used in this work which will be here called “Profile A” and “Profile B” respectively. Both profiles are centered along the constant magnetic field surface at B_{res} and have a thickness of $\Delta B = \pm 0.01\text{T}$ (refer to fig. 2a).

The power absorbed by the plasma is expected to be proportional to the square of the electric field magnitude in the wave [3, 17]. However, modeling the microwave propagation in the plasma would require a wave module, thus in order to simplify the problem, the electric field distribution in a circular

waveguide in vacuum was used to scale the power deposition profile A.

In this geometry, the dominant mode is the transverse electric mode TE₁₁, which produces a non-axisymmetric electric field. In order to use it as a scale rule, it has been averaged azimuthally, and normalized. Following this procedure fig. 4a was obtained. The region here shown is the full volume of the plasma source, whereas in the rest of the domain no power is deposited. Profile A is used in this study for the nominal simulation scenario.

To compare and study the sensitivity to the absorption profile, a second power deposition profile (profile B) was assumed. Fig. 4b shows a constant volumetric power absorption along the magnetic field surface centered in B_{res} , with a thickness of $\delta_{res} \approx 5\text{mm}$.

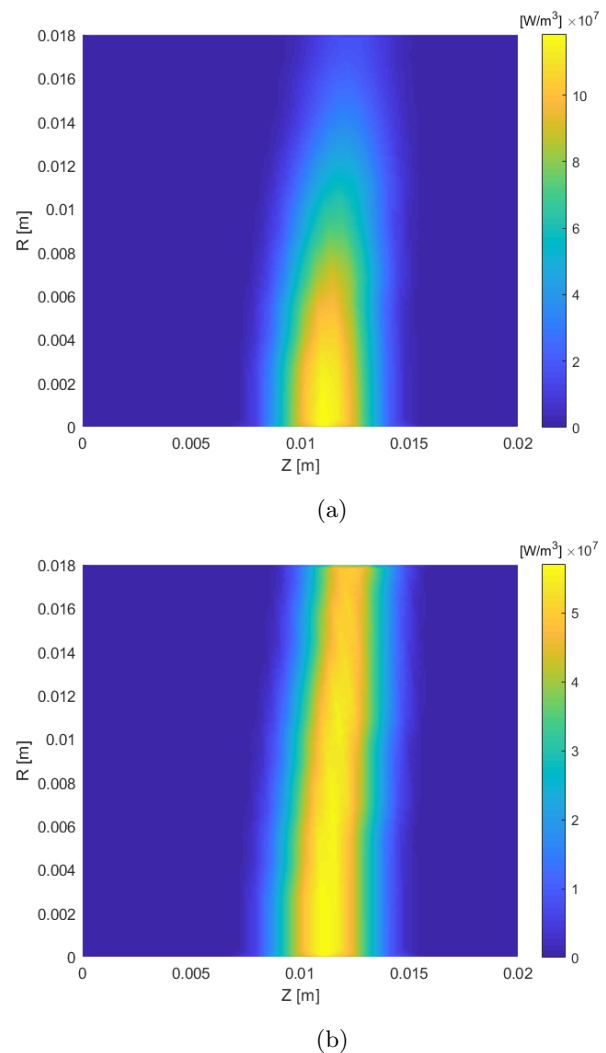


Figure 4: Thruster chamber region with Gaussian smoothed power deposition profiles Q_a for a total deposited power of $P_a = 200\text{W}$. (a) Power deposition profile A. (b) Power deposition profile B.

While the self-consistent Q_a profile requires solving the EM field, previous simulations of ECRT thruster suggest that a profile like A or B represents approximately the main characteristics of the absorption profile in the whole simulation domain [17]. Thus by studying these, we expect to understand the main aspects of the plasma transport and to be able to assess the influence of the Q_a profile as it will be shown in section 4.2. As stated above, future work will revisit this assumption and compute the absorption profile with a full wave, non-axisymmetric code.

4 RESULTS AND DISCUSSION

In section 4.1 the main plasma transport features are first analyzed for the nominal power deposition profile (Profile A) described in section 3.1, whereas the effects and the main differences induced by using profile B are discussed in section 4.2. For both cases the working point $P = 200\text{W}$ and $\dot{m}_p = 2.5\text{mg/s}$ and the same magnetic topology is chosen. Then a parametric analysis of power and mass flow rates is carried out only for the nominal profile A in section 4.3 where power and mass flow rate are varied in a set of 10 simulations.

All the plasma transport 2D maps here discussed are those obtained at steady state conditions, which is reached after $t_{ss} = 0.4\text{ms}$ (being $t = 0\text{ms}$ the time at which the fluid-pic models start to being solved together). The depicted plots correspond to averaged quantities for a time period of 0.125ms . Furthermore, in order to alleviate boundary effects, the simulation domain has been cropped and only the region up to $z = 0.08\text{m}$ and $r = 0.035\text{m}$ is kept in this work.

4.1 Discharge physics

Referring to fig. 4a, the main effect of concentrating the electron heating region towards the axis is an increased electron temperature in that region, which then tends to spread along the affected magnetic field lines. This spread happens because of the very high electron mobility in the parallel direction and is well visible in fig. 5a. Going towards higher radii, T_e decreases because of the reduced power deposited, limited electron mobility in the perpendicular direction and higher collisions rates due to the higher density of heavy particles (fig. 5b and 5c).

The plasma density profile (see fig. 5c) is influenced by the electron temperature T_e , the plasma potential ϕ (fig. 5d) and the neutral density. Starting from the axis, the density increases radially up to a maximum of 10^{19}m^{-3} because of the increased neutral density (being the injection closer) and moderately high T_e , then decreases again in the proximity of the wall due to recombination, as shown in fig. 5b.

As a consequence of the electron temperature and density behaviour, the electron pressure $P_e = n_e T_e$,

shows a peak at an intermediate radius of the plasma source region which then elongates towards the plume.

Electron pressure on the backplate as well as the ion momentum flux on the thruster walls along the z direction are responsible for the pressure thrust at the thruster walls, here defined as in equation 2.

$$F_p = \sum_s \int_{\partial\Omega_w} (n_s T_s \mathbf{1}_z \cdot \mathbf{1}_n + m_s n_s u_{zs} \mathbf{u}_s \cdot \mathbf{1}_n) dS \quad (2)$$

Where the subscripts ‘‘s’’ refer to the heavy species. $\partial\Omega_w$ is the thruster wall surface and m_s is the heavy species particle mass.

In fig. 5g the plasma pressure can be visualized as well as its gradient, where the latter presents a dominant radial component in the overall domain. This component plays a fundamental role in the electron perpendicular momentum balance, which in turn, define the electron azimuthal current density $j_{\theta e}$, which can be approximated as in equation 3:

$$j_{\theta e} \approx -\frac{\chi}{1 + \chi^2} \mu_e \left(\frac{\partial p_e}{\partial \mathbf{1}_\tau} - e n_e \frac{\partial \phi}{\partial \mathbf{1}_\tau} \right) \quad (3)$$

where $\mu_e = e/(m_e \nu_e) = \sigma_e/(n_e e)$ is the electron parallel mobility, $\chi = \omega_{ce}/\nu_e = \mu_e B$ is the Hall parameter, and where the collisions term $j_{\theta c}$ and $j_{\theta i}$ have been neglected being their contribution small.

Referring to equation 3, being the perpendicular electric field small, $j_{\theta e}$ will be mainly dictated by the perpendicular pressure gradient. This is well visible in fig. 5f which represents the $j_{\theta e}$ contributions to the magnetic force per electron. Here two regions can be distinguished, identified by the change in sign of $j_{\theta e}$ and consequently in direction of the magnetic force. One produces a positive magnetic force along z (thrust), the other produces a negative one (drag). The latter being at smaller radii also represents a smaller volume, thus has a less important role. The integral in the full domain of the magnetic force will give the magnetic thrust as in equation 4.

$$F_m \approx \int_V -j_{\theta e} B_r dV \quad (4)$$

Where $j_\theta \approx j_{\theta e}$ since the ion azimuthal current density $j_{\theta i}$ contribution results to be negligible. Thus, the total Force F exerted on the thruster, will be given by the sum of the pressure and magnetic thrust: $F = F_p + F_m$.

Finally, the electric force balances both the magnetic force and the pressure gradient and is essentially the only force balancing the pressure gradient in the parallel direction. The potential (fig. 5d) features a maximum inside the plasma source on the axis, and then it slowly decreases as the electrons expands in the magnetic nozzle, giving rise to the ion acceleration. We observe a second increasing potential region in the top left corner as a peak of around 15V . The creation of this high potential region is probably to be attributed to the vicinity of

the boundary conditions, which create a magnetically shielded region in this corner, and the quasi-neutrality of the model. Close to the thruster exit plane, the electrons are still strongly magnetized, thus it's difficult for them to access the top left corner region, limiting the plasma density. In order to keep quasi-neutrality, being the ions not constrained by magnetic field lines, a potential must rise to prevent them for reaching this region. Notwithstanding this, some experimental evidences exist that the electric potential may not decay monotonically in the transverse direction of a magnetic nozzle [29, 30], which could be explained by a non-zero ion thermal energy [31]. Further research will analyze this aspect of the simulation in detail.

4.2 Effect of the Q_a profile

The majority of the considerations discussed in section 4.1 are still applicable for the power deposition profile B, with some differences.

The immediate effect of introducing a different Q_a profile, is to produce a change in the electron temperature distribution, this is visible in fig. 5h. For this case, the electron temperature spreads uniformly across the domain keeping a value between 3.4–5eV, and a low gradient pointing towards higher radii.

This fact radically change the plasma density distribution and consequently the electron pressure gradient (refer to figs. 5j and 5n), in particular the plasma density appears to be more uniform in the plasma source and the peak density is positioned at $R = 0$ mm. The electron pressure, in contrast with what found for profile A, is now smoother and finds its maximum at the axis of symmetry. This creates a pressure gradient term $\partial p_e / \partial 1_{\top}$ that always points in the outward direction, thus also $j_{\theta e}$ does not change its sign (refer to fig. 5m). On the contrary, three drag regions are present in the plasma plume. These again seem to be mainly due to the behaviour of the pressure gradient in the corresponding regions, but it is not clear whether these are due to numerical noise or an actual phenomenon.

Finally, also the j_i current follows a different behaviour (fig. 5l) in contrast with the nominal case, with ion streamlines that feature a larger curvature in the outward direction. This, as visible in fig. 5k, is probably due to the missing high radial component of the electric field in the plasma source whereas a stronger radial component exists close to the exit plane. Instead for both Q_a profiles, because of the low magnetic field divergence, the ion streamlines appear to be still closely following the magnetic field lines in the far plume.

This analysis suggests that the temperature gradient and distribution may have an important role in the plasma expansion along a magnetic nozzle. Further analysis in this aspect will be presented in a future work.

Lastly, in tab. 4.2 can be found a summary of

the thruster performances obtained for the two Q_a profiles.

	Q_a profile A	Q_a profile B
F	11.6 mN	9.5 mN
F_m	51.7%	46.6%
F_p	48.3%	53.4%
η_d	93.3%	87.4%
η_u	86.5%	80.5%
η_p	48.9%	43.4%
η_e	29.5%	22%
η_c	46.6%	50.6%
η_F	13.6%	9.1%

Where F_m and F_p are expressed as percentages of the total thrust F .

Concerning the efficiencies they are defined as follows. The divergence efficiency is the ratio of ion kinetic power in the z direction by the total ion kinetic power $\eta_d = P_{zi\infty} / P_{i\infty}$, the subscript ∞ refers to the free loss boundaries. $\eta_u = \dot{m}_{i\infty} / \dot{m}_p$ is the utilization efficiency. $\eta_p = I_{\infty} / I_{bound}$ is the production efficiency, defined as the ratio between the ion current to the free loss boundaries (I_{∞}) and the total ion current to all the boundaries (I_{bound}). $\eta_e = P_{p\infty} / P_a$ is the energy efficiency which is the ratio between the plume power at the free loss boundaries (thermal and kinetic power) divided by the deposited power. The conversion fraction is instead $\eta_c = P_{i\infty} / P_{p\infty}$, and finally, $\eta_F = F^2 / (2\dot{m}_p P_a) \approx \eta_u \eta_e \eta_c \eta_d$ is the typical thrust efficiency.

From tab. 4.2, it appears that while the percentage of magnetic thrust and pressure thrust over the total thrust, accounts for both cases about 50%, the performance of the thruster obtained with profile A are better than the other case for each of the specified indicators but the conversion fraction.

The lower divergence efficiency of profile B can be attributed to the high radial electric field at the exit plane, which in turn is a consequence of the less localized power deposition at the axis. Whereas as appears from fig. 5i, the lower T_e causes the neutrals to extend further and with higher density in the plume, resulting also in a lower η_u .

On the other side, because of the high electron temperature in the plume of profile A and since the electron thermal power represents the majority of the beam power (see fig. 7b), the energy efficiency results to be higher for this case, with the drawback of having a lower conversion fraction.

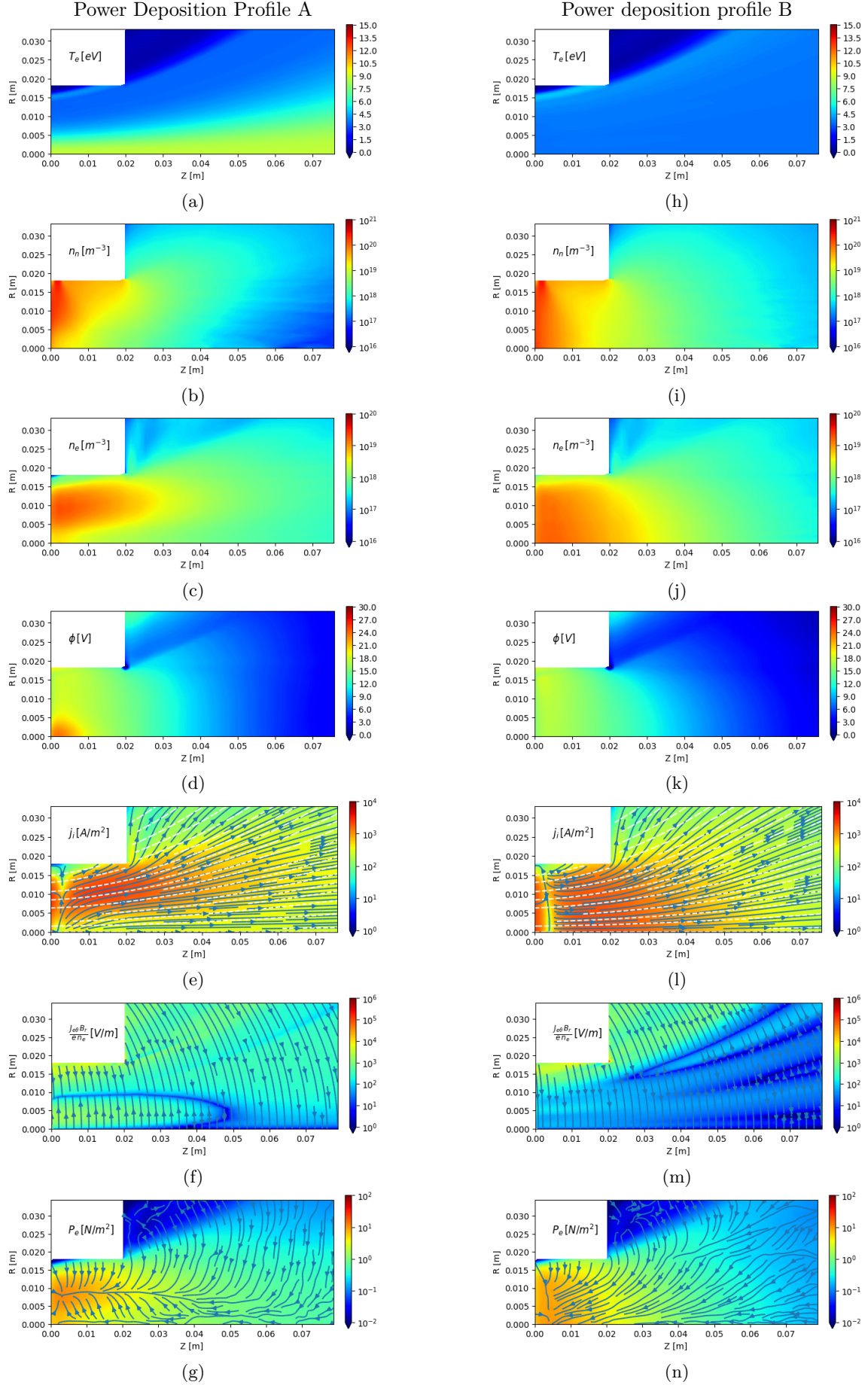


Figure 5: Comparison of the main transport parameters for the two power deposition profiles. Left: power deposition profile A. Right: power deposition profile B.

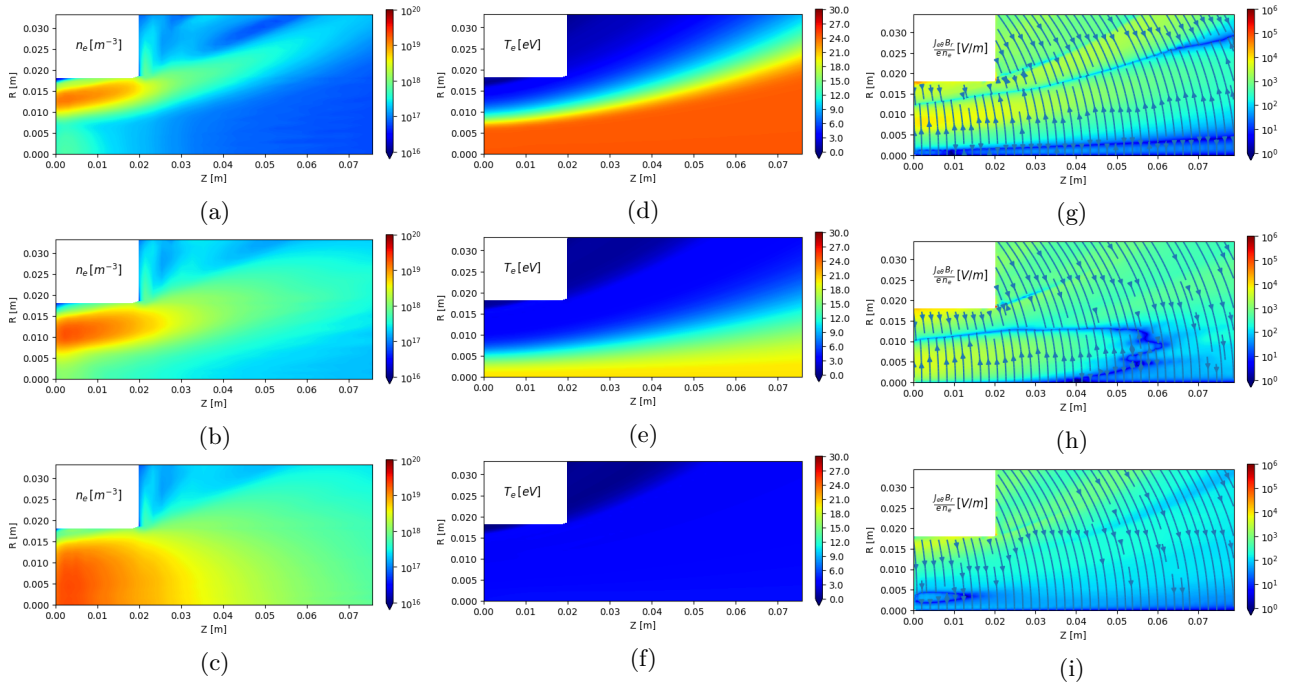


Figure 6: Plasma density n_e (a-b-c), electron temperature T_e (d-e-f) and magnetic force per electron (g-h-i) profiles, obtained at $P_a = 200\text{W}$ for mass flow rates of $\dot{m}_p = 1\text{mg/s}$, $\dot{m}_p = 2\text{mg/s}$ and $\dot{m}_p = 3\text{mg/s}$ respectively.

4.3 Parametric analysis

The effects on the plasma transport due to the variations of the mass flow rate at a fixed coupled power (200W) are now analyzed for the nominal power deposition profile A.

In fig.6(a-c) it is shown the behaviour of the plasma density when the propellant mass flow rate is varied between $\dot{m}_p = 1 - 3\text{mg/s}$ of Xenon. Similarly to what was seen in section 4.1 the density and the electron temperature are strictly correlated. This is particularly visible in fig. 6a and 6d where the high density region is compressed towards large radii, implying an increase of electron temperature for smaller radii. For all the working points analyzed in this study, the electron temperature peak ranges between 4.5-25eV, results in line with what is found experimentally for other ECR thrusters in similar working points. [10, 32]

Being the mass flow rate low and the injection radial, and given the large electron temperature, the majority of the neutrals are ionized before reaching the region close to the axis, for this reason increasing \dot{m}_p leads to a larger high density region, for which the peak reaches the axis at $\dot{m}_p = 3\text{mg/s}$ as for the power deposition case B.

Interesting is the behaviour of $j_{\theta e}$ in response to \dot{m}_p changes, which as discussed in section 4.2, is correlated with the density and temperature profiles. Referring to fig. 6 (g-i), this becomes evident at low \dot{m}_p , the region contributing negatively to the thrust expands into the plume because of the strong pressure gradient extending towards higher z . The opposite situation is found at $\dot{m}_p = 3\text{mg/s}$, the negative

thrust region almost disappears, thanks to the pressure forming a single axial peak with lower gradients, which in turn also leads to a lower $j_{\theta e}$ in the plume.

Although it is possible that in a self-consistent model, the microwave accessibility to the plasma (and thus the power deposition pattern) is altered by the change in mass flow rate, affecting globally the discharge characteristics, we see that very similar profiles to the ones found above can be obtained when the power is decreased from $P_a = 300 - 100\text{W}$ keeping a fixed mass flow rate of $\dot{m}_p = 2\text{mg/s}$. These two control parameters play an approximately opposite role. In fact, the main parameter which determines the thruster performances is the power to mass flow rate ratio, which can be expressed as energy per injected particle:

$$E_p = \frac{P_a m_{Xe}}{\dot{m}_p e} \quad [\text{eV/particle}] \quad (5)$$

Where m_{Xe} is the Xenon molecular mass in kg and e is the electron charge. In figs. 7a - 7c are shown the typical performance indicators plotted against the energy per particle E_p . It appears that, apart from outliers, the expected performances for a given E_p can be estimated directly from these plots without the need of new simulations.

Referring to fig. 7a, the thrust efficiency η_F results to be mainly influenced by the effect of η_u , which decreases fast at low energy per particle, dropping from 0.9 to 0.6. This is an expected result since if more propellant is injected without increasing in turn the power, the lower is going to be the propellant utilization.

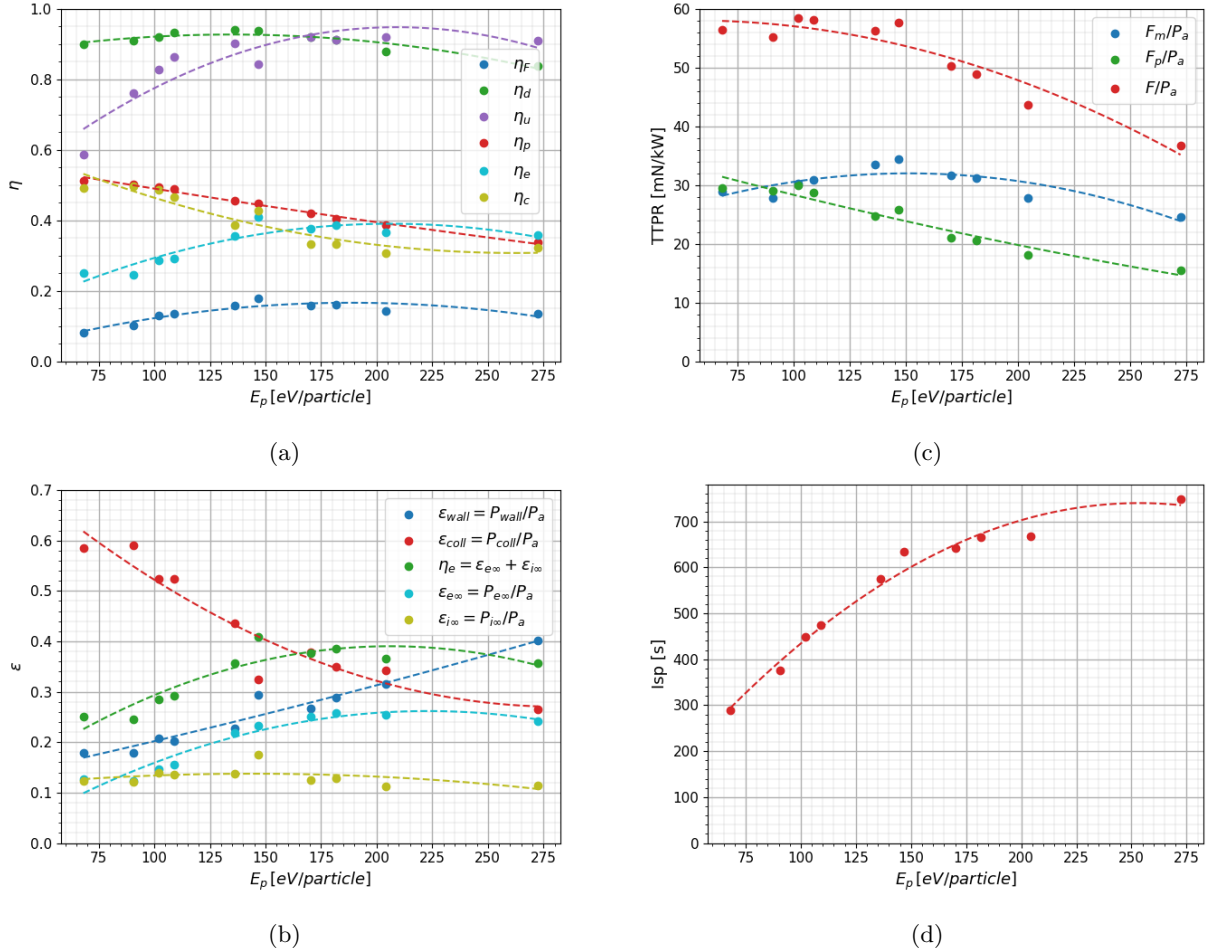


Figure 7: Primary performance indicators varying with the energy per particle E_p : Efficiencies (a), normalized losses and powers (b), Thrust to power ratios (TTPR) for magnetic and pressure thrust (c), Specific impulse (Isp) (d).

The divergence efficiency η_d , on the other hand, results to be very high in the whole range, staying between 80% and 90%, this is due to the characteristic shape of the ion streamlines seen in fig. 5e, whereas the fact that it decreases at high energy per particle can be explained by the density profile seen in fig. 6a, where the majority of the density and thus ion current is concentrated at high radii where the beam divergence is higher. Concerning the production efficiency η_p , it can vary between approximately 40% and 50%, its increase at low deposited power is due to the decreased ion current going to the walls as visible from fig. 7b. Furthermore it is found that the major cause of energy losses is represented by collisions and in particular excitation collisions. This happens especially at low levels of E_p where they can represent up to 60% of the input power.

Interestingly, the low conversion fraction η_c indicates that the expansion in the magnetic nozzle is far from over in the domain used in the present simulations. As the expansion continues farther downstream, it is expected that additional magnetic thrust, Isp, and efficiency will be generated and a

higher conversion fraction will be reached. This seems to be more relevant the higher E_p , as shown in fig. 8. This behaviour is typical of magnetic nozzle thrusters, in fact as evidenced by experimental results, the ions are found to be still accelerating even at a distance of 200mm from the thruster exit plane [33, 34].

Fig. 7c shows the TTPR (Thrust To Power Ratio) respect to the energy per particle. We see that at a fixed power, the total thrust decreases with the increase of energy per particle (decrease of mass flow rate). It appears also that the main contribution to the decrease is given by the faster decrease of pressure thrust. While the magnetic thrust initially increases with E_p in the range explored, the decrease of the magnetic thrust at higher E_p values could be explained by the larger negative thrust region seen in fig. 6g. Furthermore, the percentage of magnetic thrust to the total power can change at different working points, varying from 67% to 48%, values that are in line with the 60% found by ONERA in the coaxial ECRT measurements [35].

Finally, from figs 7a-7c different optimal opera-

tion points can be identified. If the maximum thrust efficiency is required, the energy per particle should be positioned between $E_p = 150 - 200\text{eV/particle}$, where a $\eta_F \approx 17\%$ can be obtained. Although a clear maximum is not yet reached in the total thrust in fig. 7c, it is expected that for a fixed P_a , a sufficiently large increase of \dot{m}_p will eventually lead to a drop in T_e and a decrease in thrust. Thus if a higher thrust is requested, the mass flow rate should be increased up to reaching a $E_p = 75 - 125\text{ eV/particle}$. The opposite happens for the specific impulse where the optimum should be positioned in the vicinity of $E_p = 275\text{ eV/particle}$.

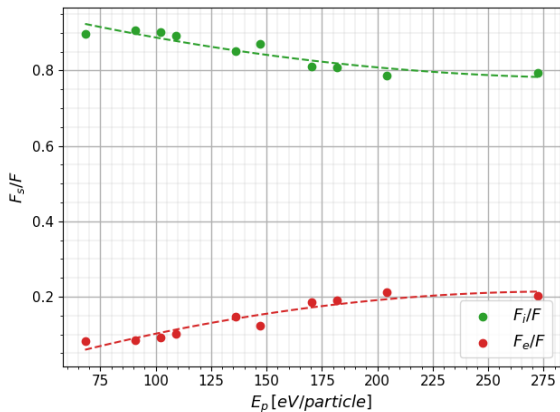


Figure 8: Electrons and ions contributions to thrust calculated at the free loss boundaries.

5 CONCLUSIONS

A Hybrid PIC-fluid model of the axisymmetric plasma discharge developed in an ECR circular waveguide thruster was used to simulate a novel thruster design under development at UC3M. The analysis identified the patterns of the main plasma transport quantities for two different power deposition profiles, and how these and the expected thruster performance change when the propellant mass flow rate and deposited power are varied.

The results point out how the proposed power deposition maps strongly affect the electron temperature profile, leading to global changes in density, pressure and potential distribution in the plasma source, consequently affecting the overall plasma discharge.

The electron temperature gradient presents two different trends: a high peak on the axis of symmetry with a strong gradient pointing radially out or a peak in the proximity of the thruster walls with an almost homogeneous but lower temperature in the bulk plasma. The effects are visible in the main terms of the momentum equation namely the magnetic force and pressure gradient. The electron pressure can extend axially or radially, altering the magnitude and direction of $j_{\theta e}$. The magnetic force on the electrons varies accordingly and can present a region of neg-

ative contribution to thrust depending on the pressure gradient direction respect to the magnetic field lines. The resulting potential alters the shape of the ion streamlines allowing them to cross the magnetic field lines from the top or from the bottom.

The parametric analysis has shown that the determining parameter is the energy per particle. It was seen that, when this figure is increased, the negative electron magnetic thrust density region grows and that the plasma is pushed towards higher radii. Furthermore, the main expected trends in the thruster figures of merit have been presented, showing results close to experimental data and pointing out that a big part of the injected power is lost in collisions and thermal electron power. The latter suggests the need of increasing the simulation domain size because of incomplete ion acceleration in the far plume especially at high energy per particle levels.

The work presented here represents a preliminary step in the understanding of the physics behind the ECR circular waveguide thruster, and serves to point out some of the limitations of the current model. In particular, it was shown the need of a wave module capable of simulating the $m = \pm 1$ mode in a cylindrical plasma domain, so that self-consistent simulations are obtained. Furthermore other aspects of the physics, believed to be important, will need to be included in the model, such as an anisotropic electron temperature and the effect of the diamagnetic field associated with the $j_{\theta e}$ currents. These together with an improved modeling of the far field boundary conditions are believed to be fundamental for an analysis closer to reality and will be subject of future works.

ACKNOWLEDGMENTS

The authors want to thank the developers of HYPHEN, in particular A. Domínguez-Vázquez and J. Zhou. This work has been supported by the PROMETEO project, funded by the Comunidad de Madrid, under Grant reference Y2018/NMT-4750 PROMETEO-CM.

References

- [1] D.M. Goebel and I. Katz. *Fundamentals of Electric Propulsion: Ion and Hall Thrusters*. Jet Propulsion Laboratory, Pasadena, CA, 2008.
- [2] R.G. Jahn. *Physics of Electric Propulsion*. Dover, 2006.
- [3] Thomas H Stix. *Waves in plasmas*. Springer Science & Business Media, 1992.
- [4] J.A. Bittencourt. *Fundamentals of plasma physics*. Springer, Berlin, Germany, 2004.
- [5] D. B. Miller and E. F. Gibbons. “Experiments with an electron cyclotron resonance plasma accelerator”. In: *AIAA Journal* 2.1 (Jan. 1964), pp. 35–41. ISSN: 0001-1452, 1533-385X. DOI: 10.2514/3.2210. URL: <https://doi.org/10.2514/3.2210>.
- [6] D.B. Miller, E.F. Gibbons, and P. Gloersen. “Cyclotron resonance propulsion system”. In: *Electric Propulsion Conference*. 1962, p. 2.
- [7] G.F. Crimi, A.C. Eckert, and DB Miller. *Microwave Driven Magnetic Plasma Accelerator Studies (Cyclops)*. Tech. rep. General Electric Company, Space Sciences Laboratory, Missile and Space Division, 1967.
- [8] J.C. Sercel. “Electron-cyclotron-resonance (ECR) plasma acceleration”. In: *AIAA 19th Fluid Dynamics, Plasma Dynamics and Lasers Conference*. 1987.
- [9] J.C. Sercel. “Simple model of plasma acceleration in a magnetic nozzle”. In: *21st International Electric Propulsion Conference*. Vol. 1. 1990.
- [10] J.C. Sercel. “An experimental and theoretical study of the ECR plasma engine”. PhD thesis. California Institute of Technology, 1993.
- [11] J. Jarrige et al. “Characterization of a coaxial ECR plasma thruster”. In: *44th AIAA Plasma-dynamics and Lasers Conference, San Diego*. 2013.
- [12] F. Cannat et al. “Experimental geometry investigation of a coaxial ECR plasma thruster”. In: *Proc. of the 34th Int. Electric Propulsion Conf.(Kobe-Hyogo, Japan)*. 2015, pp. 2015–242.
- [13] F. Cannat et al. “Optimization of a coaxial electron cyclotron resonance plasma thruster with an analytical model”. In: *Physics of Plasmas* 22.5 (2015), p. 053503.
- [14] E.B. Hooper. “Plasma flow resulting from electron cyclotron resonance heating on a magnetic hill”. In: *Physics of Plasmas* 2 (1995), p. 4563.
- [15] T. Lafleur. “Helicon plasma thruster discharge model”. In: *Physics of Plasmas* 21.4 (2014), p. 043507.
- [16] Alvaro Sánchez-Villar et al. “PIC/fluid/wave Simulations of the Plasma Discharge in an ECR Plasma Thruster”. In: *36th International Electric Propulsion Conference*. IEPC-2019-633. Vienna, Austria: Electric Rocket Propulsion Society, 2019.
- [17] A. Sánchez-Villar et al. “Coupled plasma transport and electromagnetic wave simulation of an ECR thruster”. In: *Plasma Sources Science and Technology* (submitted for publication).
- [18] D. Packan et al. “The MINOTOR H2020 project for ECR thruster development”. In: *35th International Electric Propulsion Conference*. IEPC-2017-547. Electric Rocket Propulsion Society, 2017.
- [19] Adrián Domínguez-Vázquez. “Axisymmetric simulation codes for Hall effect thrusters and plasma plumes”. PhD thesis. Universidad Carlos III de Madrid, Leganés, Spain, 2019.
- [20] Daniel Pérez-Grande. “Fluid modeling and simulation of the electron population in Hall effect thrusters with complex magnetic topologies”. PhD thesis. Universidad Carlos III de Madrid, Leganés, Spain, 2018.
- [21] Adrián Domínguez-Vázquez et al. “Analysis of the plasma discharge in a Hall thruster via a hybrid 2D code”. In: *36th International Electric Propulsion Conference*. IEPC-2019-579. Vienna, Austria: Electric Rocket Propulsion Society, 2019.
- [22] Filippo Cichocki et al. “Hybrid 3D model for the interaction of plasma thruster plumes with nearby objects”. In: *Plasma Sources Science and Technology* 26.12 (2017), p. 125008. ISSN: 0963-0252.
- [23] Filippo Cichocki et al. “Application of EP2PLUS 3D code to plasma thruster plumes and discharges”. In: *EPIC workshop*. London, UK, 2018.
- [24] Daniel Pérez-Grande et al. “Analysis of the numerical diffusion in anisotropic mediums: benchmarks for magnetic field aligned meshes in space propulsion simulations”. In: *Applied Sciences* 6.11 (2016), p. 354.
- [25] D. Pérez-Grande et al. “Development updates for a two-dimensional axisymmetric hybrid code for plasma thruster discharges”. In: *35th International Electric Propulsion Conference*. IEPC-2017-201. Atlanta, GA: Electric Rocket Propulsion Society, 2017.
- [26] E. Ahedo and V. de Pablo. “Combined effects of electron partial thermalization and secondary emission in Hall thruster discharges”. In: *Physics of Plasmas* 14 (2007), p. 083501.

- [27] E. Ahedo, J.M. Gallardo, and M. Martínez-Sánchez. “Effects of the radial-plasma wall interaction on the axial Hall thruster discharge”. In: *Physics of Plasmas* 10.8 (2003), pp. 3397–3409.
- [28] Jiewei Zhou et al. “Numerical treatment of a magnetized electron fluid within an electromagnetic plasma thruster code”. In: *Plasma Sources Science and Technology* 28.11 (2019), p. 115004.
- [29] C. Charles. “High density conics in a magnetically expanding helicon plasma”. In: *Applied Physics Letters* 96.5 (2010), pp. 051502–051502.
- [30] Justin M Little and Edgar Y Choueiri. “Electron Demagnetization in a Magnetically Expanding Plasma”. In: *Physical review letters* 123.14 (2019), p. 145001.
- [31] Mario Merino and Eduardo Ahedo. “Influence of Electron and Ion Thermodynamics on the Magnetic Nozzle Plasma Expansion”. In: *IEEE Transactions on Plasma Science* 43.1 (2015), pp. 244–251. ISSN: 0093-3813. DOI: 10.1109/TPS.2014.2316020.
- [32] T. Lafleur et al. “Electron dynamics and ion acceleration in expanding-plasma thrusters”. In: *Plasma Sources Science and Technology* 24.6 (2015), p. 065013.
- [33] J. Jarrige et al. “Investigation on the ion velocity distribution in the magnetic nozzle of an ECR plasma thruster using LIF measurements”. In: *35th International Electric Propulsion Conference*. IEPC-2017-382. Atlanta, GA: Electric Rocket Propulsion Society, Fairview Park, OH, 2017.
- [34] S Correyero et al. “Plasma beam characterization along the magnetic nozzle of an ECR thruster”. In: *Plasma Sources Science and Technology* 28.9 (2019), p. 095004. DOI: 10.1088/1361-6595/ab38e1.
- [35] T. Vialis, J. Jarrige, and D. Packan. “Separate measurements of magnetic and pressure thrust contributions in a magnetic nozzle electron cyclotron resonance plasma thruster”. In: *Space Propulsion Conference*. 499. Seville, Spain, May 2018.